The Astrophysical Journal, 867:21 (11pp), 2018 November 1 https://doi.org/10.3847/1538-4357/aadf38
© 2018. The American Astronomical Society. All rights reserved.

Revealing Dusty Supernovae in High-redshift (Ultra)Luminous Infrared Galaxies through Near-infrared Integrated Light Variability

Haojing Yan[1], Zhiyuan Ma[1], John F. Beacom[2,3,4], and James Runge[1]
[1] Department of Physics and Astronomy, University of Missouri-Columbia, MO, USA; yanha@missouri.edu, zmzff@mail.missouri.edu, jmr24f@mail.missouri.edu
[2] Department of Physics, The Ohio State University, OH, USA; beacom.7@osu.edu
[3] Department of Astronomy, The Ohio State University, OH, USA
[4] Center for Cosmology and AstroParticle Physics (CCAPP), The Ohio State University, OH, USA
Received 2018 June 18; revised 2018 September 3; accepted 2018 September 3; published 2018 October 25

Abstract

Luminous and ultra-luminous infrared galaxies ((U)LIRGs) are rare today but are increasingly abundant at high redshifts. They are believed to be dusty starbursts, and hence should have high rates of supernovae (multiple events per year). Due to their extremely dusty environment, however, such supernovae could only be detected in rest-frame infrared and longer wavelengths, where our current facilities lack the capability of finding them individually beyond the local universe. We propose a new technique for higher redshifts, which is to search for the presence of supernovae through the variability of the integrated rest-frame infrared light of the entire hosts. We present a pilot study to assess the feasibility of this technique. We exploit a unique region, the "IRAC Dark Field" (IDF), that the *Spitzer Space Telescope* has observed for more than 14 years in 3–5 μm. The IDF also has deep far-infrared data (200–550 μm) from the *Herschel Space Observatory* that allow us to select high-redshift (U)LIRGs. We obtain a sample of (U)LIRGs that have secure optical counterparts, and examine their light curves in 3–5 μm. While the variabilities could also be caused by AGNs, we show that such contaminations can be identified. We present two cases where the distinct features in their light curves are consistent with multiple supernovae overlapping in time. Searching for supernovae this way will be relevant to the *James Webb Space Telescope* (*JWST*) to probe high-redshift (U)LIRGs into their nuclear regions where *JWST* will be limited by its resolution.

Key words: dust, extinction – galaxies: active – galaxies: starburst – submillimeter: galaxies – supernovae: general

1. Introduction

Luminous and ultra-luminous infrared galaxies (LIRGs and ULIRGs; hereafter "(U)LIRGs") have high IR luminosity (integrated over rest-frame 8–1000 μm) of $L_{\rm IR} > 10^{11}$ and $>10^{12}\,L_{\odot}$, respectively. It is widely believed that (U)LIRGs are starbursts, and that their strong IR emissions are mostly due to the dust-reprocessed UV photons from their large numbers of young stars. On the other hand, (U)LIRGs usually also harbor AGNs, which often makes it difficult to attribute their major IR power source solely to starbursts (see Lonsdale et al. 2006b). It is important to distinguish these hypotheses or, more likely, to determine their fractional contributions to the (U)LIRG power and how those may change with redshift. Although (U)LIRGs are rare today, they are more common at high redshifts (e.g., Le Floc'h et al. 2005; Magnelli et al. 2013), which make them relevant to the global picture of galaxy evolution across cosmic time.

A decisive way to determine the fraction of (U)LIRGs' power supplied by starbursts would be to measure their rates of supernovae (SNe). If they are indeed dominantly powered by starbursts, (U)LIRGs should have high star formation rates (SFRs; >10 and $>100\,M_{\odot}\,{\rm yr}^{-1}$ for LIRGs and ULIRGs, respectively), and hence should also have high rates of SNe. For ULIRGs, the rate $r_{\rm SN}$ is estimated to be $\gtrsim$2–3 events yr^{-1} (van Buren & Greenhouse 1994; Mattila & Meikle 2001). However, due to the severe dust obscuration, such SNe would have to be searched for in the radio or IR.

VLBI detections of radio SNe and SN remnants in the ULIRG Arp 220 and the LIRG Arp 299 (e.g., Lonsdale et al. 2006a; Pérez-Torres et al. 2009; Romero-Cañizales et al. 2011, 2014; Bondi et al. 2012; Varenius et al. 2017, and references therein) lend strong support to high $r_{\rm SN}$ in (U)LIRGs. For example, Lonsdale et al. (2006a) derive $r_{\rm SN} \sim 4$ events yr^{-1} for Arp 220, which implies a sufficient SFR to account for its $L_{\rm IR}$ without resorting to AGN. VLBI imaging, however, still cannot be applied to (U)LIRGs beyond the local universe. IR surveys have also discovered a few tens of SNe in local (U)LIRGs (e.g., Maiolino et al. 2002; Cresci et al. 2007; Mattila et al. 2007; Kankare et al. 2008; Miluzio et al. 2013; Kool et al. 2018), including multiple SNe in the same galaxies (e.g., Kankare et al. 2012, 2014). Two main conclusions have been drawn from these results: (1) (U)LIRGs indeed have a high rate of SNe embedded by dust, which are not visible to optical surveys. (2) The current IR surveys must still be missing a large fraction of dusty SNe close to the nuclear region of the host galaxies due to both the extreme dust extinctions and the much decreased survey sensitivities when working against the bright background. Unfortunately, these IR surveys also do not go beyond the local universe.

As an alternative to discovering SNe individually, we propose to reveal them through the variability of the integrated IR light of the host. This method can be easily applied to high-z, because it requires only high-precision differential photometry. As far as we are aware, no search of this type has been performed, and a pilot study is needed to assess the prospects for present instruments and especially for the *James Webb Space Telescope* (*JWST*). To set the scale required, a supernova peaking at $M \sim -19$ mag within a host of $M \sim -21$ mag (i.e., $m \sim 22.4$ mag at $z \approx 1$) would increase the host brightness by $\sim$0.16 mag, which should be detectable by current facilities. If a (U)LIRG has multiple SNe per year, they could overlap in time and result in even larger variability. Admittedly, finding evidence of dust-embedded SNe in this way is inferior to

resolving them individually in terms of the follow-up applications of the SNe; nevertheless, it is still a powerful means to probe the nuclear regions that the activities are expected to be the most violent and yet are the most difficult to penetrate. The only major contaminations would be AGNs, which are known to vary with typical amplitudes of a few tenths of magnitude (e.g., Peterson 2001).

In this paper, we exploit a unique field known as the "IRAC Dark Field" (hereafter "IDF"; see Krick et al. 2009). Since its launch in 2003, the *Spitzer Space Telescope* has been observing this area for the calibration of its InfraRed Array Camera (IRAC; Fazio et al. 2004), producing a deep field of $\sim$13′ in radius. The IDF (R.A. = $17^{\rm h}40^{\rm m}$, decl. = $68^{\rm o}40'$, J2000) is close to the North Ecliptic Pole, and is in a region of the lowest zodiacal background (hence "dark"). During the cryogenic phase (2003 October to 2009 May), all four IRAC channels (3.6, 4.5, 5.8, and 8.0 μm) were used. After the coolant depletion ("warm-mission" phase), the 3.6 and 4.5 μm channels (hereafter "Ch1" and "Ch2," or "Ch1/2") have continued observations without any significant loss of sensitivity. The IDF is the only region on the sky with long-duration (>14 years) monitoring data in 3–5 μm (sampling rest-frame near-IR up to $z \approx 3.5$), and its early data ($\sim$2 years) were already of unprecedented time baseline such that it inspired a search for Population III supernovae, albeit with null results (Frost et al. 2009). The IDF is ideal for our purpose here because of two additional reasons: it has (1) hundreds of (U) LIRGs revealed by the far-IR (FIR) observations from the *Herschel Space Observatory* and (2) medium-deep *Chandra* X-ray observations for AGN diagnostics.

Our paper is organized as follows. We present the data in Section 2, and describe the selection of variable objects in Section 3. The analysis of these variable objects is given in Section 4, which is followed by a discussion in Section 5. A brief summary is given in Section 6. We use AB magnitudes throughout the paper, and adopt $\Omega_M = 0.27$, $\Omega_\Lambda = 0.73$ and $H_0 = 71\ {\rm km\ s^{-1}\ Mpc^{-1}}$.

2. Data and Analysis

We describe the data used in this study, which span a wide range from X-ray to FIR.

2.1. Spitzer *IRAC Data*

Our analysis is based on the IRAC Ch1/2 images from 2003 October through 2017 December. The retrieved data include the "Basic Calibrated Data" (BCDs), which are single exposures with the major instrumental effects removed by the standard *Spitzer* Science Center (SSC) data reduction pipeline, and the so-called "post-BCD" (PBCD) products, which are the combined results from the BCDs within a single observation sequence known as a "Astronomical Observation Request" (AOR). As the observations in Ch1 and Ch2 are simultaneous (but in two adjacent fields), the PBCD products of each AOR contain the mosaics (and other diagnostic files) in both Ch1 and Ch2.

The AOR designs depend on the goals of the calibrations, and thus are not uniform: they can be different in the frame time of single exposures, the total duration, the field position, the spatial coverage, etc. We only kept the AORs whose single exposures have a frame time $\geqslant$100 s. This resulted in 424 and 635 AORs in the cryogenic and the warm-mission phases, respectively, i.e., a total of 424+635 = 1059 PBCD mosaics at 1059 epochs in both Ch1 and Ch2. Figure 1 shows the epoch map of these AORs. These mosaics have median integration times ranging from 96.8 to 2516.8 s/pixel, and the majority have either 374.4–387.2 s/pixel (30.8%) or 561.6–580.8 s/pixel (46.4%) in Ch1, and either 387.2 s/pixel (30.8%) or 484.0 s/pixel (41.1%) in Ch2, respectively. The pixel scale of these PBCD products is 0.″6, which is about half of the native pixel sizes.

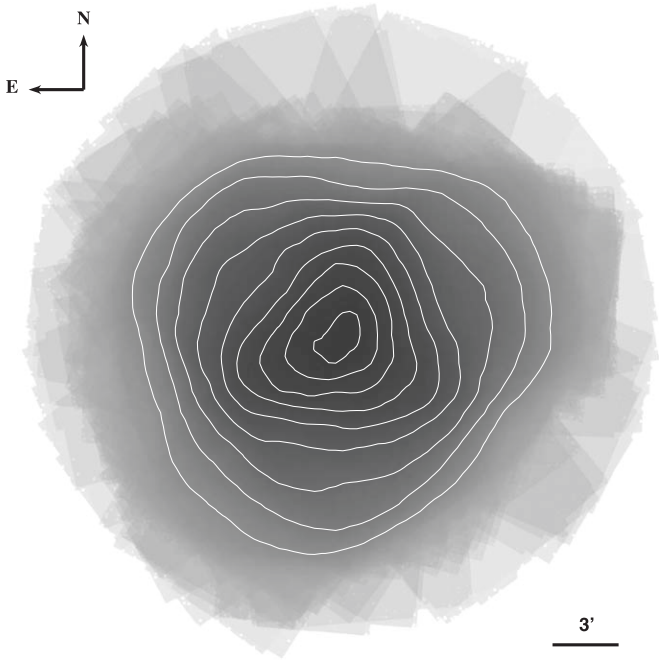

Figure 1. IRAC Ch1 epoch map in the IDF ($\sim$13′ radius), based on the 1059 AORs (Section 2.1). The contours are shown from 100 to 900 epochs in a 100 epoch step-size. The Ch2 epoch map is similar.

We ran SExtractor (Bertin & Arnouts 1996) on each PBCD mosaic for photometry, using the associated uncertainty map (i.e., specifying the flux uncertainty at each pixel) as the rms map. We adopted `MAG_AP` with circular apertures of 2″, 3″, 4″, 5″, and 6″ in diameter. The individual source catalogs were matched to generate the "light-curve catalog" of 1059 epochs in Ch1/2. We found that the data in the first 37 AORs of the warm-mission phase (MJD 55035 through 55115) likely suffered from photometric zero-point errors, and hence excluded these data. The final number of useful epochs is 1022.

2.2. Herschel *SPIRE Data*

The *Herschel* Spectral and Photometric Imaging Receiver (SPIRE; Griffin et al. 2010) periodically observed the IDF region (in the 250, 350, and 500 μm bands) for calibration throughout its mission (from 2009 September to 2013 April). In total, there are 151 AORs of various coverage and central pointings, mostly large or small mapping scans with durations ranging from about eight minutes to two hours.

We retrieved and analyzed these data using the *Herschel* Interactive Processing Environment (HIPE; Ott 2010). The instrumental effects have already been removed by the *Herschel* data reduction pipeline, which result in the "Level 1" products. Our reduction was to stack these products of the 151 AORs. SPIRE always observed its three bands in the same field of view, and hence we obtained the mosaics and their noise maps in all three bands. The final mosaics extend an

area of ∼0.88 deg^2, with the pixel scales of 6″, 10″, and 14″ in 250, 350, and 500 μm, respectively.

We generated a band-merged catalog using 250 μm as the detection band, following the general procedure of Wang et al. (2014). The detection was done on the 250 μm map using StarFinder (SF; Diolaiti et al. 2000), which is an iterative source finding program that can deal with images of significant source blending problem. The detection was done iteratively using a PSF-fitting technique so that faint sources around bright ones could be included. We adopted the following SF parameters: "SNR_thresh" of 1.5, "Correction thresh" of 0.7, and "Deblending distance" of 0.7 × FWHM, where FWHM was set to 18.″15 for the 250 μm band. The positions of these 250 μm sources were sent to the task sourceExtractorSimultaneous in HIPE to do photometry in all three bands simultaneously. We used a Gaussian Point Response Function with the FWHM value set to 18.″15, 25.″15, and 36.″30 at 250, 350, and 500 μm, respectively (see Swinyard et al. 2010). The routine generated flux densities, as well as their uncertainties based on the noise maps. For the latter, we added in quadrature a constant confusion noise of 5 mJy to obtain the final estimates of the uncertainties. In total, we detected 1759 SPIRE sources within the IRAC coverage, 208 of which have S/N ⩾ 5.

2.3. Chandra *X-Ray Data*

The IDF has been observed by the *Chandra* ACIS-I camera for ∼100 ks, and these observations are described in Krick et al. (2009). Following the procedures similar to theirs, we reduced these data independently using the *Chandra* Interactive Analysis of Observations software (CIAO, v4.9; with CALDB 4.7.0). All observations were reprocessed using the chandra_repro script, which corrects for image defects (such as hot pixels and cosmic-ray afterglows) and does background cleaning before creating a final event list. The processed event files for each observation were then merged using merge_obs, similar to merge_all used by Krick et al. (2009) except that it folds in the reproject_aspect script. We then ran wavdetect on the merged event list with the "mexican hat" wavelet functions on size scales from 1 to 8. The merged event list was converted into flux images through the use of eff2evt in three energy bands (soft: 0.5–1.2 keV; medium: 1.2–2.0 keV; hard: 2.0–7.0 keV). The positions from the wavdetect run were fed to roi to create a source and background region for each object. Source and background measurements were then made on the individual flux images using dmstat. In total, we extracted 121 sources within the IRAC coverage.

2.4. *WIYN and* HST *Optical Data*

We have been observing the IDF using the One-Degree Imager (ODI) in $u'g'r'i'z'$ at the WIYN telescope. For this study, we used the i'-band data obtained on 2017 March 29 and April 1, with the purpose of providing the positional priors for the SPIRE source counterpart identification. These images, totaling two hours of integration, were first reduced by the ODI pipeline to remove the instrumental effects and to calibrate their astrometry based on the GAIA Data Release 1. We then stacked them using the SWarp software (by E. Bertin; V2.38.0). The mosaic has reached 25.2 mag (5σ), has the PSF FWHM of 0.″65, and has an rms accuracy of 30 mas in astrometry.

The IDF has also been observed by the *HST* Advanced Camera for Surveys (ACS) in the F814W-band at 2-orbit depth (see Krick et al. 2009). Here, we only use them to obtain the morphologies of interesting sources when necessary, and hence we rely on the per-visit stacks (pixel scale 0.″05) contained in the pipeline-reduced data directly retrieved from the *HST*.

3. Searching for Variability

As our interest is the SNe of the (U)LIRGs and the possible contamination due to AGNs, here we limit our variability search to only the IRAC counterparts of the SPIRE sources (potential (U) LIRGs) and the *Chandra* sources (potential AGNs).

3.1. *Optical/IR Counterparts of SPIRE Sources and Chandra Sources*

We first identified the optical counterparts of the aforementioned 208 S/N ⩾ 5 SPIRE 250 μm sources, using our own Counterpart Identifier tool ("CIDer"; Z. Ma & H. Yan 2018, in preparation) developed following the general PSF-fitting methodology as in Yan et al. (2014). For a given 250 μm source, which might be the blended product of multiple objects, the ODI i'-band image is used to locate the possible contributors to its flux. CIDer only identifies the major contributors, i.e., the i'-band objects that contribute the bulk of the 250 μm flux. This is achieved by iteratively fitting the 250 μm PSF at the positions of the potential contributors, which is appropriate because the 250 μm image has so coarse a resolution (PSF FWHM ∼18″) that all sources are point-like. We required that a major contributor must contribute ⩾25% of the 250 μm flux. In total, CIDer identified 201 i'-band objects as the major contributors to 148 250 μm sources. We then cross-matched these i'-band objects with those in the IRAC light-curve catalog, using a matching radius of 1″. All these 201 i'-band objects have IRAC counterparts.

The identification of the IRAC counterparts of the 121 *Chandra* sources was straightforward, which was done by cross-matching to the IRAC light-curve catalog using a matching radius of 1″. In total, 71 *Chandra* sources have IRAC counterparts.

3.2. *FIR Sample, X-Ray Sample, and Control Sample*

To ensure the most reliable detection of IRAC variability, we require that an object must have photometry over at least 100 epochs in either Ch1 alone or Ch2 alone. The variability was searched through these three samples:

(1) Among the 201 i'-band major contributors to 148 *Herschel*/SPIRE 250 μm sources (i.e., potential (U) LIRGs) within the IRAC coverage, 96 have ⩾100 epochs of photometry and thus comprise our FIR sample.
(2) Among the 71 X-ray sources (i.e., potential AGNs) within the IRAC coverage that have IRAC counterparts, 67 satisfy the same criterion and hence comprise our X-ray sample. There are 8 objects in common with the FIR sample.
(3) A control, "field" sample is constructed by selecting the IRAC sources that are >21″ away from any SPIRE 250 μm sources and >3″ away from of any X-ray sources. This includes 1987 objects that have ⩾100 epochs of photometry.

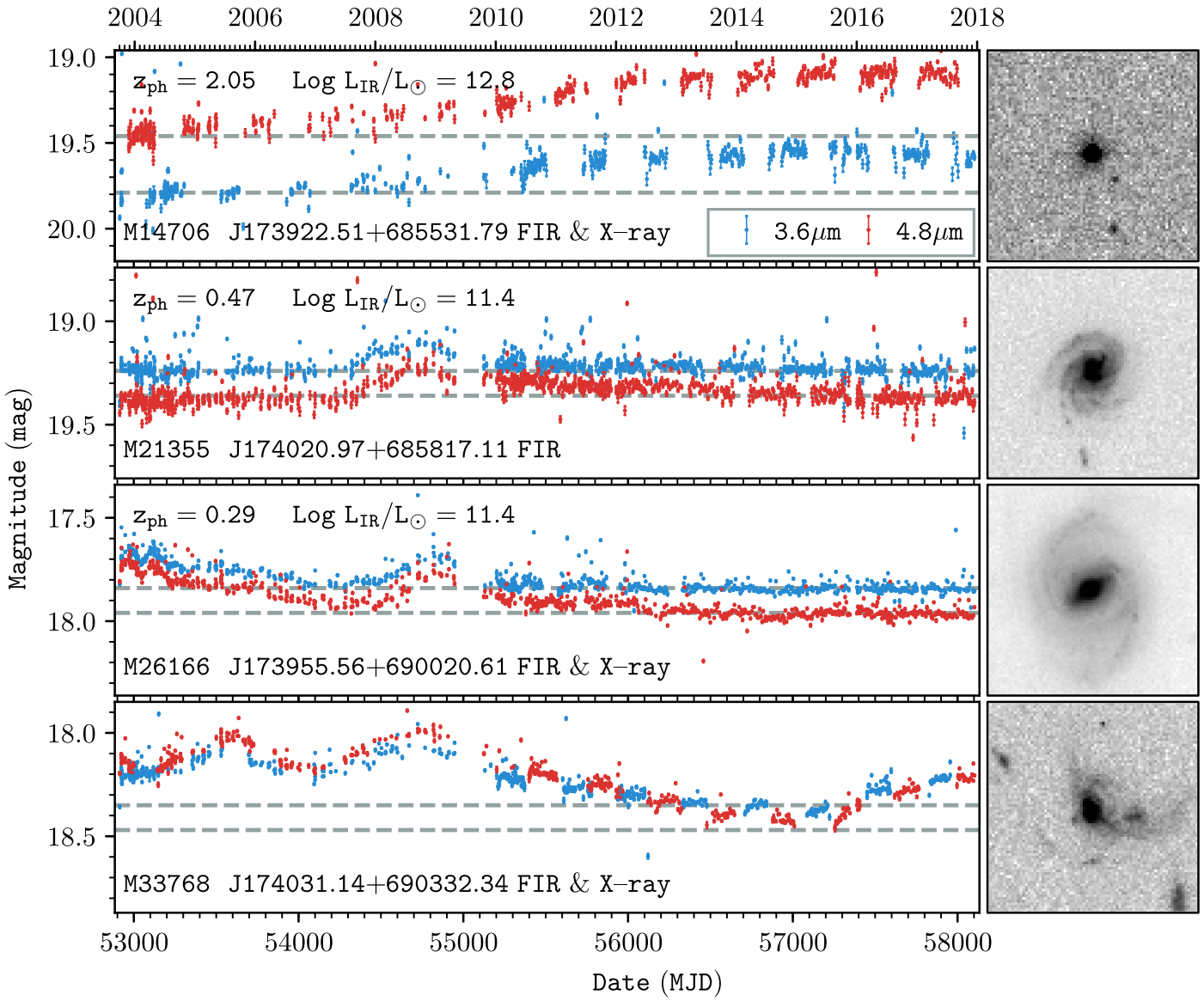

Figure 2. IRAC Ch1 (blue) and Ch2 (red) light curves of the four variable sources in the FIR sample (indicated by "FIR"), with their IDs and names (IAU convention) noted. The three objects that are also in the X-ray sample are labeled by "X-ray." The magnitudes are based on circular apertures of 4″ diameter, and aperture corrections of −0.36 and −0.39 mag have been applied to Ch1 and Ch2, respectively. The *HST* F184W image stamps (6″ × 6″) to the right show their morphologies. The first three objects have z_{ph} and therefore their L_{IR} can be calculated (see Section 3.4, Figures 4 and 5), and these values are also labeled. The last one currently does not have z_{ph}.

3.3. Variable Objects

We adopted the $d = 4''$ MAG_AP values as the benchmark, and used those measured in other apertures for verification once a candidate was found. A candidate variable source was selected using these criteria: (1) its brightness continuously changes over >30 days, (2) the peak-to-valley variation is >0.1 mag, and (3) the average photometric error over the changing period is <0.05 mag. In addition, its light curve and images were visually examined to confirm its legitimacy.

In the end, 4 and 21 variable objects were found in the FIR and the X-ray samples, respectively. Three of these objects are in common, resulting in 22 unique sources in total. In contrast, none of the 1987 objects in the control sample have *comparable* variability. Figure 2 shows the light curves and the ACS F814W images of the variables in the FIR sample. For comparison, Figure 3 shows the light curves of the 18 variables in the X-ray sample (i.e., excluding the three duplicates from the FIR sample). Note that these Ch1/2 magnitudes are based on $d = 4''$ aperture but have been applied the corrections of −0.102 and −0.105 mag in Ch1 and Ch2, respectively, to convert to the "total" magnitudes. These values are obtained by interpolating between the aperture corrections of $d = 3.''6$ and $d = 4.''8$ provided in the IRAC Instrument Handbook.

3.4. IR and X-Ray Luminosities

We then determine whether these 22 variable objects reside in (U)LIRGs and/or AGNs, for which we need their redshifts to calculate their IR and/or X-ray luminosities. None of them have spectroscopic redshifts, and we adopt six photometric redshifts (z_{ph}) available from the SDSS DR14. For the rest, we derive their z_{ph} on our own by fitting their spectral energy distributions (SEDs). To best match the existing SDSS z_{ph}, we

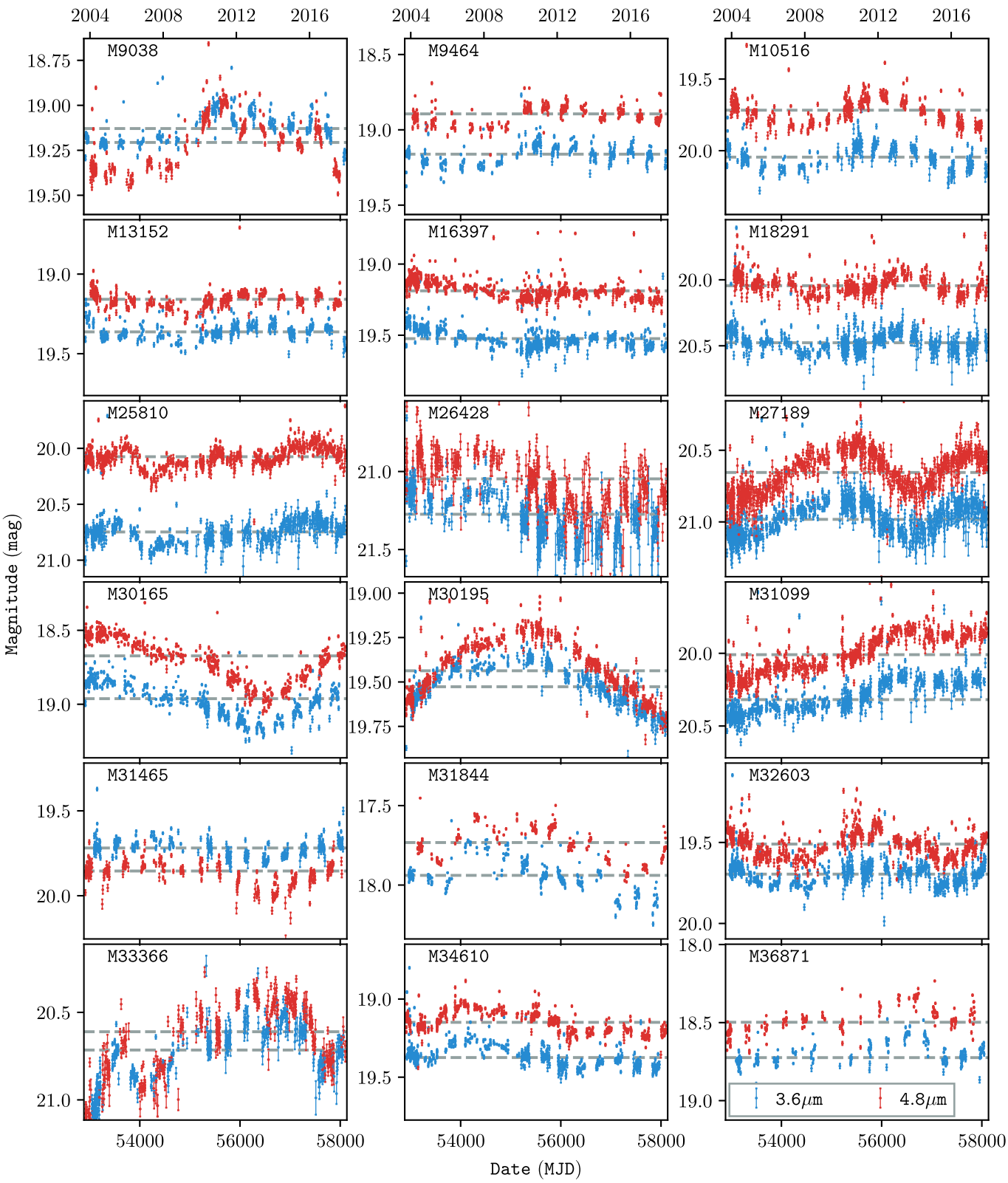

Figure 3. IRAC Ch1 (blue) and Ch2 (red) light curves of the 18 objects in the X-ray sample (with their ID noted), excluding the three already shown in Figure 2. Magnitudes are the same as in Figure 2.

confine these SEDs to the optical regime and use the SDSS photometry. Seven objects have to be excluded from this analysis because they are not detected in the SDSS due to their faintness, one of which is in both the FIR and the X-ray samples and the other six are in the X-ray sample. In the end, we have nine objects that need their $z_{\rm ph}$ derived.

An X-ray AGN does not necessarily show AGN signatures in other wavelengths. Therefore, we first treat these nine

objects as "normal" galaxies dominated by starlight in the optical, and fit them using the EAZY software (Brammer et al. 2008). An important reason to use EAZY is that it allows Bayesian prior(s) to assign very low weight to unreasonable $z_{\rm ph}$ solutions, which is particularly important in our case because galaxies bright enough to be detected in the SDSS should be at $z \lesssim 0.8$. Specifically, we use its `prior_R_extend.dat`, and treat the SDSS r'-band as the R-band.[5] We obtain a satisfactory fit for four of them. For the five objects that do not fit well from the above, we consider the possibility that their optical light is dominated by AGNs. We fit them using the LePhare software (Arnouts et al. 1999; Ilbert et al. 2006), which includes QSO/AGN templates. We note that no prior is applied in the LePhare run. As it turns out, all five objects can be fit reasonably well.

To check the consistency of our $z_{\rm ph}$ with the SDSS results, we also repeat the same procedure for the aforementioned six objects that already have SDSS $z_{\rm ph}$. We find that they can all be well fit using EAZY with galaxy templates, and the differences between the SDSS $z_{\rm ph}$ and ours have mean $\langle \Delta z/(1+z) \rangle = 0.04$. Therefore, we believe that combining these two sets of $z_{\rm ph}$ is reasonable. Figure 4 summarizes the SED fitting results for all 15 objects.

For those in the FIR sample, we construct their FIR SEDs using the SPIRE photometry based on the fractional contributions of the major contributors, and derive $L_{\rm IR}$ by fitting to the templates of Chary & Elbaz (2001), following Ma & Yan (2015). M33768 is not detected in the SDSS and hence is not considered. Figure 5 shows the FIR SED fitting results for the other three objects. All four IRAC variable objects in the FIR sample have $L_{\rm IR} > 10^{11}\,L_{\odot}$, qualifying as (U)LIRGs.

For those in the X-ray sample, we calculate their X-ray luminosities ($L_{\rm X}$) based on the *Chandra* photometry. This is done using $L_{\rm X} = f_X \times 4\pi D_L^2$, where $f_{\rm X}$ is the flux density over rest-frame 0.2–10 keV and D_L is the luminosity distance. To obtain $f_{\rm X}$, a power-law SED in the form of $I_\nu \approx \nu^{-\alpha}$ is fit to the flux densities at different energy bands, and the best fit is integrated over rest-frame 0.2–10 keV. We find that they all have $L_{\rm X} \geqslant 10^{42}\,{\rm erg^{-1}\,s^{-1}\,cm^{-2}}$ and thus fall within the nominal range of X-ray AGNs.

Table 1 summarizes the properties of all these objects discussed above. For the sake of completeness, the table also lists those that do not yet have $z_{\rm ph}$ estimates. These latter objects are also included in the discussions below as potential (U)LIRGs and AGNs.

4. Interpretation

While it is natural to attribute the variabilities seen in the X-ray sample to AGN variability, our focus here is to examine whether the four variable objects in the FIR sample (see Figure 2) could be due to multiple SNe.

4.1. SNe versus AGNs

It is plausible that the variability of M21355 is caused by multiple SNe, as it is the only non-X-ray source (among the four) and hence very likely does not harbor an AGN. However, the other three need more examination because they are X-ray AGNs as well.

[5] Such a prior sets the likelihood of redshift for a given magnitude; as an example, the adopted function at $m = 20$ mag peaks at $z = 0.24$.

We suggest that the variability of M26166 is also likely due to multiple SNe for two reasons. First, both M26166 and M21355 have blue Ch1−Ch2 colors. This means that their 3–5 μm emission cannot be dominated by AGNs (e.g., Stern et al. 2005), which then leaves multiple SNe as the plausible explanation for their variabilities. In contrast, most other variables in the X-ray sample (15 out of 18) have red Ch1−Ch2 colors (i.e., consistent with AGN SEDs), and only three are exceptions (M9038, M31466, and M33366).

Second, both M26166 and M21355 have a long "quiet" phase ($\gtrsim$6 years), which is different from those of the other 19 variable objects in the two samples combined. We argue that this is actually an expected feature in our current search. If a (U)LIRG maintains a constant, high $r_{\rm SN}$ all the time, the events cannot be easily detected from the variability because the host is always at an elevated flux level due to the SNe overlapping in time. On the other hand, a (U)LIRG could also achieve the same average rate by erupting a few times more SNe over a short period and then remaining "quiet" over a period longer by the same factor. In this case, the variability becomes more significant, which could be what we see in M21355 and M26166.

By these arguments, the variabilities of M14706 and M33768 in the FIR sample are most likely due to AGNs, like others in the X-ray sample. In particular, this should not be surprising for M14706, as it is one of the five objects whose optical SEDs are better fit with quasar/AGN templates, and should be a quasar based on its point-like morphology (see Figure 2).

4.2. Consistency with SNe Cause

Accepting that M21355 and M26166 could have multiple SNe, we now examine how well their light curves can be explained. Unfortunately, this cannot be done quantitatively with the current data, because we do not know the types of SNe involved, let alone their relative fractions. Nevertheless, we can still qualitatively examine whether the amplitudes and the durations of the variabilities could be consistent with the SNe interpretation.

Figure 6 shows their "net" Ch1 variations after subtracting the host fluxes as determined over the "quiet" periods. We model the variations by composing the average K-band light curve template of Type II SNe derived by Mattila & Meikle (2001), which is represented by two power-law functions before and after the maximum. While this approach does not capture the detailed behaviors of the real light curves, the template is sufficient for such a toy model. The average peak absolute magnitude of this template is $K = -18.6$ mag in Vega system, or equivalently, $K_{AB} = -16.73$ mag.

At $z \approx 0.3$–0.5, Ch1 is close to the rest-frame K-band; while it samples slightly longer wavelengths than K-band, we ignore this small difference. The modeling is done by combining an arbitrary number of light curve templates (time-dilated at the source redshift) at arbitrary times. This results in a large number of plausible model sets, one of which is shown in Figure 6 for each source to explain one of the most prominent features. The features span over ~800 days in the observer's frame, and can be reasonably modeled by a stack of 60 and 80 templates for M21355 and M26166, respectively. This translates to $r_{\rm SN}$ of ~40–47 events yr^{-1} (in rest-frame), which is qualitatively consistent with the expectation that we are

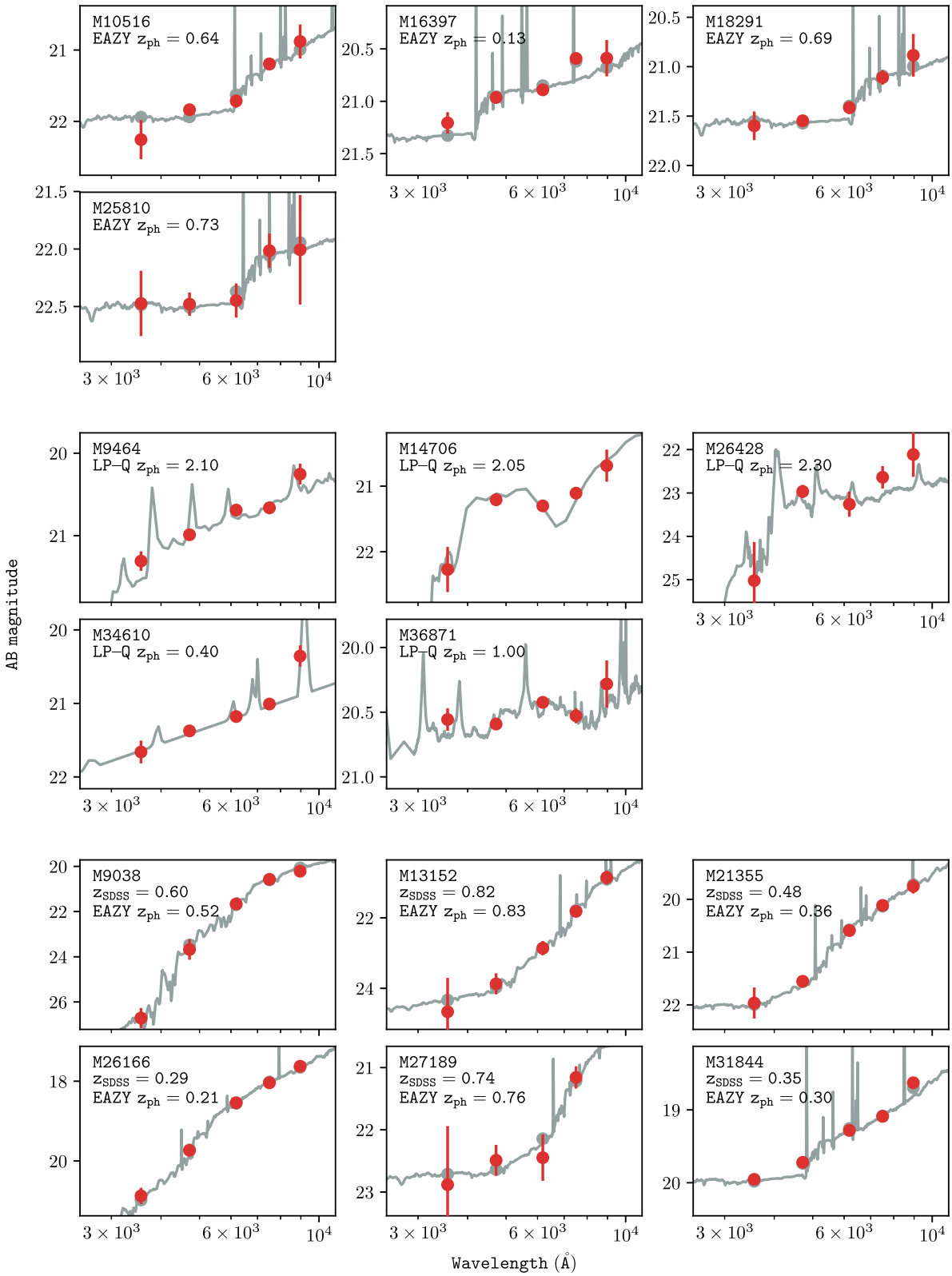

Figure 4. Optical SED fitting and z_{ph} derivation for the 15 objects that have SDSS photometry. The red dots with error bars are the data points, and the gray curves are the best-fit models. The first four rows show the nine objects that do not have existing SDSS z_{ph}, for which we derive z_{ph} independently. Among these, four objects (shown in the first two rows) can be fit by galaxy models using EAZY (results labeled as "EAZY z_{ph}"), and the other five (shown in the next two rows) can only be fit by AGN/QSO models using LePhare (results labeled as "LP-Q z_{ph}"). To check the consistency, the six objects with existing SDSS z_{ph} (shown in the last two rows and values labeled with "z_{SDSS}") are also fit using the same procedure, and they can all be fit by galaxy models using EAZY. The mean difference between the two sets is $\langle \Delta z/(1+z) \rangle = 0.04$.

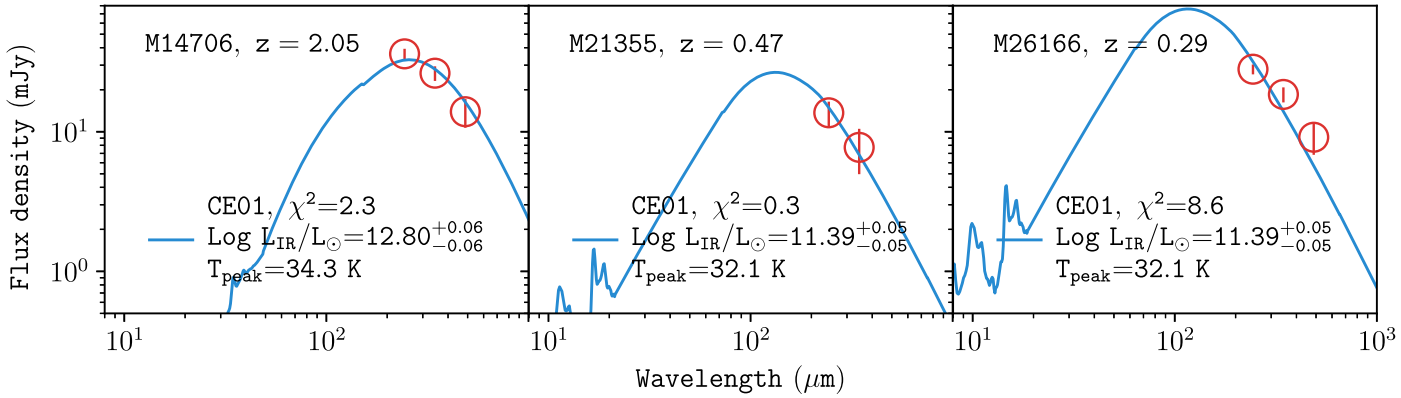

Figure 5. FIR SED fitting of the three objects in the FIR sample that have z_{ph}. The red circles with error bars are the SPIRE photometry using the appropriate fractional contributions from the identified major optical counterparts, and the blue curves are the best models from CE01. The derived L_{IR} values are labeled. We also calculate the peak dust temperatures (T_{peak}) based on the best-fit models, which are also labeled.

observing an elevated rate over a short period of time as discussed in Section 4.1 above.

We emphasize that such a toy model is only meant to demonstrate that the features in the light curves can be explained by multiple SNe but not to deduce any detailed properties of the SNe. Many important factors have to be omitted because the current data do not warrant the consideration of such details. For example, we do not consider the population of "super luminous SNe" (at least two magnitudes more luminous than the adopted template) that have been known for two decades (Gal-Yam 2012), which would decrease the required r_{SN}. We also neglect dust extinction in near-IR, which could still be significant and could affect the brightness of the involved SNe. Nevertheless, it is particularly encouraging that using just one specific SN light curve can explain the features, and one can imagine that allowing different types of SNe would only work better.

5. Discussion

Strictly speaking, the analysis in Section 4 only shows that the variabilities in M21355 and M26166 are consistent with the SNe interpretation but does not definitely prove it, the latter of which probably could only be claimed if the SNe were detected individually. However, we are able to rule out the AGN variability as their cause based on the Ch1/2 color of the hosts and the light curve behaviors, and hence leave the SNe explanation as the likely alternative. Multiple SNe have been detected individually in at least two local LIRGs (Arp 299 and IC 833; see the references in Section 1), and thus it should not be surprising that we find evidence of similar events at high redshifts.

One might question why such variabilities cannot be due to other types of transients. Among all other populations, only tidal disruption events (TDEs; see Komossa 2015, for a review), which are thought to be due to the disruption of a star falling into the supermassive black hole at a galaxy center, could possibly have IR amplitude and varying timescale comparable to SNe. TDEs emit most strongly in the X-ray to optical wavelengths, and these energetic photons could be absorbed by the dusty ISM around the black hole and re-emit in IR (see, e.g., Lu et al. 2016). Such IR "echoes" have been found for a few TDEs (Dou et al. 2016, 2017; Jiang et al. 2016, 2017; van Velzen et al. 2016) by using the *Wide-field Infrared Survey Explorer* (*WISE*) data (Wright et al. 2010) in *W1* (3.4 μm) and *W2* (4.6 μm) bands, which are close to the Ch1/2 bands used in our study. Wang et al. (2018) further present a sample of *WISE* sources that have similar variability and suggest that they could also be the IR echoes of TDEs (but see also Assef et al. 2018). More energetic TDEs have also been suggested, such as the very luminous transient in Arp 299 recently discovered by Mattila et al. (2018). However, invoking TDEs for M21355 and M26166 is problematic, because both objects would certainly require multiple TDEs to explain the features in their light curves. This would imply several events over 10 years, which is orders-of-magnitude higher than the expected rate of $\sim 10^{-5}$ yr^{-1} per galaxy (Wang & Merritt 2004; Wang et al. 2012; van Velzen & Farrar 2014; Holoien et al. 2016).[6] Therefore, we believe that TDEs are unlikely the cause. In contrast, the multiple SNe interpretation comes naturally, as it meets the expectation that (U)LIRGs should have a high rate of SNe because of their high SFR.

We emphasize that our pilot study here is the first one using variability of integrated IR light to reveal dust-embedded SNe in (U)LIRGs beyond the local universe. There have been other IR variability studies in the literature, some of which also utilize IRAC Ch1/2. A significant example is that of Kozłowski et al. (2010a), who investigated the IRAC variability of objects in the 8.1 deg^2 *Spitzer* Deep Wide-Field Survey in the Boötes field over four epochs spanning four years. Aiming at variability in general, however, they do not target (U)LIRGs, and most of their variable objects are due to AGNs. While this work has led to the serendipitous discovery of a self-obscured SN at $z \approx 0.2$ (Kozłowski et al. 2010b), the SN is not related to a (U)LIRG and its obscuration is due to its dusty circumstellar medium but not the environment. Another example is the ongoing SPitzer InfraRed Intensive Transients Survey (SPIRITS; Kasliwal et al. 2017), which searches for Ch1/2 transients in 190 nearby galaxies. SPIRITS has also led to the discovery of new SNe: Jencson et al. (2017) report two SNe in IC 2163 (not a LIRG) separated by less than two years. This survey, which does not include (U)LIRGS, is confined to the local universe (<15 Mpc) and only aims to discover transients that can be individually resolved.

[6] While there are now suggestions that TDEs could occur at a much higher rate in (U)LIRGs (Tadhunter et al. 2017), such a connection is yet to be established.

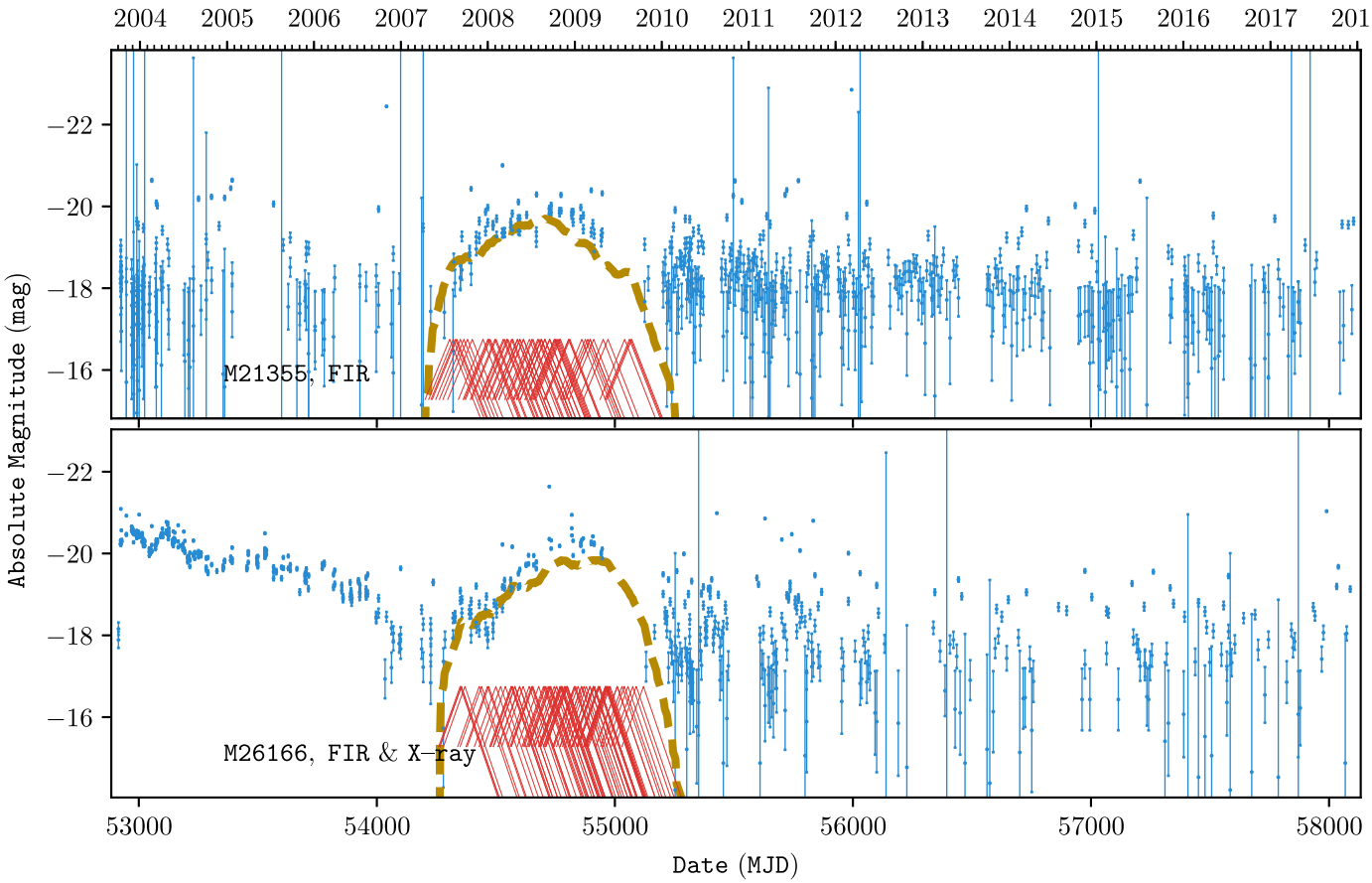

Figure 6. Net Ch1 variabilities of M21355 and M26166 derived by subtracting the host light based on their quiet phases (after 2011 for both; see Figure 2) and toy models that qualitatively explain the features of the light curves. The blue dots with error bars (calculated based on the S/N after subtraction of the host) are the data points, while the horizontal dashed gray line indicates the "zero-flux" level around which there are equal numbers of positive and negative residuals in the quiet phases (the negative residuals cannot be shown due to the magnitude scale). For clarity, the toy models are only shown for one of the most prominent features for each source. The models are constructed using the power-law *K*-band light curve template for Type II SNe as derived by Mattila & Meikle (2001). The features, which span over ∼800 days in the observer's frame, can be qualitatively explained by the combined effects (dashed golden curves) that resulted from stacking 60 and 80 templates (red curves) for M21355 and M26166, respectively.

The implication of our study can be understood in two-fold. First, we present strong supporting evidence that high-z (U)LIRGs, like their local counterparts, have a high rate of SNe. While determining $r_{\rm SN}$ is beyond the scope of this paper, it is obvious that the two cases[7] shown in Figure 4 require multiple SNe per year over the active periods. This makes (U)LIRGs ideal targets to search for high-z SNe in the rest-frame IR, which will become feasible when the *JWST* comes online in the near future. The unprecedented IR resolution and sensitivity offered by the *JWST* will easily enable us to detect such SNe individually out to any redshifts where (U)LIRGs are seen and to assemble large samples that can lead to many applications. Second, using the integrated light variability as the indicator of SNe in high-z (U)LIRGs will remain relevant in the *JWST* era because it will still be difficult for *JWST* to probe close to the nuclear regions. For example, *JWST*'s resolution at 4.4 μm (the reddest band of its NIRCam instrument) is $\sim 0\farcs17$, which corresponds to ∼1.4 kpc at $z \approx 1$–2. ULIRGs have now been found out to $z \approx 6$–7 (Riechers et al. 2013; Fudamoto et al. 2017; Strandet et al. 2017), and to sample the rest-frame *K*-band at such redshifts *JWST* will need to observe at 18–20 μm using its MIRI instrument at the resolution of $\sim 0\farcs75$, which corresponds to ∼4.2 kpc. In such cases, our method will be the only option. Of course, one would not be able to obtain a *JWST* time baseline or cadence comparable to the IDF IRAC observations, and the "quiet phase" argument presented in Section 4 would not be applicable. However, if the *JWST* monitoring is done in at least two bands, the color information can always be used to judge if the observed variability is more likely due to SNe or AGN. In addition, contemporary observations in one optical band can also greatly help the judgment, because the variability caused by dusty SNe should not be seen in optical due to the large extinction in (U)LIRGs.

Lastly, we point out that the very field of IDF is of great interest for the *JWST*. By design, the IDF is close to the North Ecliptic Pole and thus is in the continuous viewing zone (CVZ) of *JWST*, which is the narrow region within ±5° from the Ecliptic Poles.[8] For this reason, the IDF can be visited by the *JWST* at any time of the year. It will be ideal for a *JWST* monitoring program, especially when considering the fact it is the only region in the CVZ that has deep *Herschel* data revealing a large sample of high-z (U)LIRGs.

[7] We note that the other objects in the FIR sample also have hints of variabilities but are at lower levels; however, we have to differ the discussion to a forthcoming paper because our current analysis does not yet allow us to confidently assess these more subtle features in the light curves.

[8] See "*James Webb Space Telescope* User Documentation," https://jwst-docs.stsci.edu/display/JTI/JWST+Observatory+Coordinate+System+and+Field+of+Regard.

Table 1
Properties of the 22 Strongly Variable IDF IRAC Sources Studied in This Work

IAU Name	ID	Sample	z_{ph}	z_{ph}-source	Log L_{IR} ($L_\odot$)	Log L_X (erg s^{-1})	i'	Ch1	Ch2
IDFV J174002.2+685305.53	M9038	X-ray	0.60	SDSS	⋯	43.5	21.02	19.13	19.21
IDFV J174027.4+685317.25	M9464	X-ray	2.10	LP-Q	⋯	44.6	20.92	19.16	18.89
IDFV J173959.0+685343.79	M10516	X-ray	0.64	EAZY	⋯	43.4	21.55	20.05	19.72
IDFV J174027.5+685450.07	M13152	X-ray	0.82	SDSS	⋯	43.4	21.71	19.36	19.16
IDFV J173922.5+685531.91	M14706	FIR/X-ray	2.05	LP-Q	12.8	44.3	20.99	19.90	19.52
IDFV J173955.0+685617.78	M16397	X-ray	0.13	EAZY	⋯	42.0	20.60	19.52	19.19
IDFV J174048.5+685702.79	M18291	X-ray	0.69	EAZY	⋯	43.2	21.17	20.48	20.04
IDFV J174021.0+685817.00	M21355	FIR	0.48	SDSS	11.4	⋯	20.12	19.49	19.63
IDFV J173936.1+690013.98	M25810	X-ray	0.73	EAZY	⋯	42.9	22.32	20.75	20.07
IDFV J173955.6+690020.63	M26166	FIR/X-ray	0.29	SDSS	11.4	42.6	18.28	18.09	18.22
IDFV J174100.6+690027.72	M26428	X-ray	2.30	LP-Q	⋯	44.7	23.54	21.27	21.05
IDFV J174003.3+690048.26	M27189	X-ray	0.74	SDSS	⋯	43.2	22.62	20.98	20.66
IDFV J174031.3+690158.70	M30165	X-ray	⋯	⋯	⋯	⋯	23.17	18.96	18.67
IDFV J173930.4+690159.65	M30195	X-ray	⋯	⋯	⋯	⋯	22.07	19.53	19.44
IDFV J174012.9+690223.89	M31099	X-ray	⋯	⋯	⋯	⋯	22.56	20.32	20.01
IDFV J173901.1+690234.07	M31465	X-ray	⋯	⋯	⋯	⋯	22.21	19.72	19.85
IDFV J174116.7+690241.61	M31844	X-ray	0.35	SDSS	⋯	43.7	18.96	17.94	17.73
IDFV J173951.9+690302.22	M32603	X-ray	⋯	⋯	⋯	⋯	22.69	19.70	19.51
IDFV J173924.3+690318.01	M33366	X-ray	⋯	⋯	⋯	⋯	22.89	20.72	20.61
IDFV J174031.1+690332.22	M33768	FIR/X-ray	⋯	⋯	⋯	⋯	21.15	18.48	18.47
IDFV J174026.8+690353.12	M34610	X-ray	0.40	LP-Q	⋯	42.1	21.04	19.37	19.15
IDFV J173855.7+690451.92	M36871	X-ray	1.00	LP-Q	⋯	44.4	20.41	18.72	18.50

Note. The columns are: (1) IAU name, where the coordinates are based on the OID i' positions, (2) internal ID used in our IDF catalog, (3) sample(s) to which a source belongs, i.e., FIR sample, X-ray sample, or both, (4) z_{ph}, (5) the source of z_{ph}, i.e., from the SDSS, our own EAZY run using galaxy templates or LePhare run using QSO/AGN templates (LP-Q), (6) log(L_{IR}), (7) log(L_X), (8) i' magnitude as measured in the ODI image, (8) averaged Ch1 magnitude after aperture correction, and (9) averaged Ch2 magnitude after aperture correction.

6. Summary

If (U)LIRGs are mainly driven by starbursts, they should have a high rate of SNe embedded by dust. This would make them ideal "SNe factories" that can produce large SNe samples at high z if the search is done in the rest-frame IR where the dust extinction is minimal. In this study, we use the IDF 3–5 μm data, which span more than 14 years, to test this idea. We propose that such dust-embedded SNe in (U)LIRGs can be revealed by the variabilities in the integrated near-IR light of the host galaxy, which can be applied to high-z where it is difficult to discern SNe individually due to the lack of sufficient spatial resolution and/or sensitivity. Our paper demonstrates the feasibility of this method. Out of the 96 potential high-z (U)LIRGs that have the best temporal coverage (the FIR sample), we identify 4 strongly variable objects. We show that the contamination due to AGN variability can be discriminated based on information such as their colors, and present two strong cases that are consistent with multiple SNe overlapping in time. It is very likely that a future *JWST* monitoring program targeting fields of known (U)LIRGs can resolve many such SNe. However, variability study will remain the only way to probe the SN activities close to the nuclear regions where even *JWST* still lacks the resolution to resolve the SNe individually.

We acknowledge the support of the University of Missouri Research Board Grant RB 15-22 and NASA's ADAP Program under grant number NNX15AM92G. J.F.B. is supported by NSF Grant No. PHY-1714479. Part of our data processing and analysis were done using the HPC resources at the University of Missouri Bioinformatics Consortium (UMBC) and the Ohio Supercomputer Center (OSC).

ORCID iDs

Haojing Yan https://orcid.org/0000-0001-7592-7714
Zhiyuan Ma https://orcid.org/0000-0003-3270-6844

References

Arnouts, S., Cristiani, S., Moscardini, L., et al. 1999, MNRAS, 310, 540
Assef, R. J., Prieto, J. L., Stern, D., et al. 2018, ApJ, submitted (arXiv:1807.07985)
Bertin, E., & Arnouts, S. 1996, A&AS, 117, 393
Bondi, M., Pérez-Torres, M. A., Herrero-Illana, R., & Alberdi, A. 2012, A&A, 539, A134
Brammer, G. B., van Dokkum, P. G., & Coppi, P. 2008, ApJ, 686, 1503
Chary, R., & Elbaz, D. 2001, ApJ, 556, 562
Cresci, G., Mannucci, F., Della Valle, M., & Maiolino, R. 2007, A&A, 462, 927
Diolaiti, E., Bendinelli, O., Bonaccini, D., et al. 2000, Proc. SPIE, 4007, 879
Dou, L., Wang, T., Yan, L., et al. 2017, ApJL, 841, L8
Dou, L., Wang, T.-g., Jiang, N., et al. 2016, ApJ, 832, 188
Fazio, G. G., Hora, J. L., Allen, L. E., et al. 2004, ApJS, 154, 10
Frost, M. I., Surace, J., Moustakas, L. A., & Krick, J. 2009, ApJL, 698, L68
Fudamoto, Y., Ivison, R. J., Oteo, I., et al. 2017, MNRAS, 472, 2028
Gal-Yam, A. 2012, Sci, 337, 927
Griffin, M. J., Abergel, A., Abreu, A., et al. 2010, A&A, 518, L3
Holoien, T. W.-S., Kochanek, C. S., Prieto, J. L., et al. 2016, MNRAS, 455, 2918
Ilbert, O., Arnouts, S., McCracken, H. J., et al. 2006, A&A, 457, 841
Jencson, J. E., Kasliwal, M. M., Johansson, J., et al. 2017, ApJ, 837, 167
Jiang, N., Dou, L., Wang, T., et al. 2016, ApJL, 828, L14
Jiang, N., Wang, T., Yan, L., et al. 2017, ApJ, 850, 63
Kankare, E., Mattila, S., Ryder, S., et al. 2008, ApJL, 689, L97
Kankare, E., Mattila, S., Ryder, S., et al. 2012, ApJL, 744, L19
Kankare, E., Mattila, S., Ryder, S., et al. 2014, MNRAS, 440, 1052
Kasliwal, M. M., Bally, J., Masci, F., et al. 2017, ApJ, 839, 88
Komossa, S. 2015, JHEAp, 7, 148
Kool, E. C., Ryder, S., Kankare, E., et al. 2018, MNRAS, 473, 5641
Kozłowski, S., Kochanek, C. S., Stern, D., et al. 2010a, ApJ, 716, 530
Kozłowski, S., Kochanek, C. S., Stern, D., et al. 2010b, ApJ, 722, 1624
Krick, J. E., Surace, J. A., Thompson, D., et al. 2009, ApJS, 185, 85

Le Floc'h, E., Papovich, C., Dole, H., et al. 2005, ApJ, 632, 169
Lonsdale, C. J., Diamond, P. J., Thrall, H., Smith, H. E., & Lonsdale, C. J. 2006a, ApJ, 647, 185
Lonsdale, C. J., Farrah, D., & Smith, H. E. 2006b, in Astrophysics Update 2, ed. J. W. Mason (Chichester: Praxis), 285
Lu, W., Kumar, P., & Evans, N. J. 2016, MNRAS, 458, 575
Ma, Z., & Yan, H. 2015, ApJ, 811, 58
Magnelli, B., Popesso, P., Berta, S., et al. 2013, A&A, 553, A132
Maiolino, R., Vanzi, L., Mannucci, F., et al. 2002, A&A, 389, 84
Mattila, S., & Meikle, W. P. S. 2001, MNRAS, 324, 325
Mattila, S., Pérez-Torres, M., Efstathiou, A., et al. 2018, Sci, 361, 482
Mattila, S., Väisänen, P., Farrah, D., et al. 2007, ApJL, 659, L9
Miluzio, M., Cappellaro, E., Botticella, M. T., et al. 2013, A&A, 554, A127
Ott, S. 2010, in ASP Conf. Ser. 434, Astronomical Data Analysis Software and Systems XIX, ed. Y. Mizumoto, K.-I. Morita, & M. Ohishi (San Francisco, CA: ASP), 139
Pérez-Torres, M. A., Romero-Cañizales, C., Alberdi, A., & Polatidis, A. 2009, A&A, 507, L17
Peterson, B. M. 2001, in Advanced Lectures on the Starburst-AGN, ed. I. Aretxaga, D. Kunth, & R. Mújica (Singapore: World Scientific), 3
Riechers, D. A., Bradford, C. M., Clements, D. L., et al. 2013, Natur, 496, 329
Romero-Cañizales, C., Herrero-Illana, R., Pérez-Torres, M. A., et al. 2014, MNRAS, 440, 1067
Romero-Cañizales, C., Mattila, S., Alberdi, A., et al. 2011, MNRAS, 415, 2688
Stern, D., Eisenhardt, P., Gorjian, V., et al. 2005, ApJ, 631, 163
Strandet, M. L., Weiss, A., De Breuck, C., et al. 2017, ApJL, 842, L15
Swinyard, B. M., Ade, P., Baluteau, J.-P., et al. 2010, A&A, 518, L4
Tadhunter, C., Spence, R., Rose, M., Mullaney, J., & Crowther, P. 2017, NatAs, 1, 0061
van Buren, D., & Greenhouse, M. A. 1994, ApJ, 431, 640
van Velzen, S., & Farrar, G. R. 2014, ApJ, 792, 53
van Velzen, S., Mendez, A. J., Krolik, J. H., & Gorjian, V. 2016, ApJ, 829, 19
Varenius, E., Conway, J. E., Batejat, F., et al. 2017, arXiv:1702.04772
Wang, J., & Merritt, D. 2004, ApJ, 600, 149
Wang, L., Viero, M., Clarke, C., et al. 2014, MNRAS, 444, 2870
Wang, T., Yan, L., Dou, L., et al. 2018, MNRAS, 477, 2943
Wang, T.-G., Zhou, H.-Y., Komossa, S., et al. 2012, ApJ, 749, 115
Wright, E. L., Eisenhardt, P. R. M., Mainzer, A. K., et al. 2010, AJ, 140, 1868
Yan, H., Stefanon, M., Ma, Z., et al. 2014, ApJS, 213, 2